AGU PUBLICATIONS

Tectonics

RESEARCH ARTICLE
10.1002/2014TC003716

Key Points:
- Microstructural characterization of an incipient thrust fault
- Fault zone is affected by a large calcite departure compared to host sediments
- Fault frictional strength very low even if fault experienced low displacement

Correspondence to:
B. Lacroix,
bricelacroix@yahoo.fr

Citation:
Lacroix, B., T. Tesei, E. Oliot, A. Lahfid, and C. Collettini (2015), Early weakening processes inside thrust fault, *Tectonics*, *34*, 1396–1411, doi:10.1002/2014TC003716.

Received 18 AUG 2014
Accepted 3 MAY 2015
Accepted article online 7 MAY 2015
Published online 14 JUL 2015

©2015. American Geophysical Union. All Rights Reserved.

Early weakening processes inside thrust fault

B. Lacroix[1,2], T. Tesei[3,4], E. Oliot[5], A. Lahfid[6], and C. Collettini[4,7]

[1]Institut des Sciences de la Terre, Université de Lausanne, Lausanne, Switzerland, [2]Department of Earth and Environmental Sciences, University of Michigan, Ann Arbor, Michigan, USA, [3]Dipartimento di Fisica e Geologia, Università degli Studi di Perugia, Perugia, Italy, [4]Istituto Nazionale di Geofisica e Vulcanologia, Roma, Italy, [5]Institut de Physique du Globe de Strasbourg, UMR 7516, University of Strasbourg/EOST, CNRS, Strasbourg, France, [6]Unité Caractérisation Minérale, Physico-chimique et Texturale (LAB/MIN), Bureau de Recherches Géologiques et Minières, Orléans, France, [7]Dipartimento Scienze della Terra, Università Sapienza di Roma, Rome, Italy

Abstract Observations from deep boreholes at several locations worldwide, laboratory measurements of frictional strength on quartzo-feldspathic materials, and earthquake focal mechanisms indicate that crustal faults are strong (apparent friction $\mu \geq 0.6$). However, friction experiments on phyllosilicate-rich rocks and some geophysical data have demonstrated that some major faults are considerably weaker. This weakness is commonly considered to be characteristic of mature faults in which rocks are altered by prolonged deformation and fluid-rock interaction (i.e., San Andreas, Zuccale, and Nankai Faults). In contrast, in this study we document fault weakening occurring along a marly shear zone in its infancy (<30 m displacement). Geochemical mass balance calculation and microstructural data show that a massive calcite departure (up to 50 vol %) from the fault rocks facilitated the concentration and reorganization of weak phyllosilicate minerals along the shear surfaces. Friction experiments carried out on intact foliated samples of host marls and fault rocks demonstrated that this structural reorganization lead to a significant fault weakening and that the incipient structure has strength and slip behavior comparable to that of the major weak faults previously documented. These results indicate that some faults, especially those nucleating in lithologies rich of both clays and high-solubility minerals (such as calcite), might experience rapid mineralogical and structural alteration and become weak even in the early stages of their activity.

1. Introduction

Measurements of crustal stress levels in deep boreholes [*Townend and Zoback*, 2000] and analysis of earthquake focal mechanisms [*Collettini and Sibson*, 2001] suggest that many faults have an apparent friction close to the experimental Byerlee's friction $\mu \sim 0.6$–0.85 [*Byerlee*, 1978]. However, geological and geophysical evidence [*Zoback et al.,* 1987; *Suppe*, 2007; *Cubas et al.,* 2013] and some laboratory experiments on phyllosilicate-rich fault rocks [e.g., *Collettini et al.,* 2009; *Lockner et al.,* 2011; *Carpenter et al.,* 2011; *Ikari and Saffer*, 2011; *Tesei et al.,* 2012] suggest that some major faults, in all tectonic settings, are weak; i.e., they move under low resolved shear stress and/or have low apparent friction. In particular, faults along detachment sedimentary horizons, which allow the decoupling and imbrication of tectonic units in fold-thrust belts, are inferred to be extremely weak ($\mu \ll 0.6$) [*Suppe*, 2007; *Cubas et al.,* 2013].

The causes for upper crustal fault weakness are manifold: they range from time-dependent creep mechanisms of rocks such as pressure solution [e.g., *Gratier et al.,* 2013] to elevated internal fluid pressure [e.g., *Hubbert and Rubey*, 1959; *Sibson and Xie*, 1998] or to the presence of intrinsically weak minerals [e.g., *Moore and Rymer*, 2007; *Collettini et al.,* 2009]. The prolonged deformation and alteration in the core of mature fault zones are generally thought to have dramatic effects in changing the mineralogy and lowering the strength of fault rocks [e.g., *Chester et al.,* 1993; *Wintsch et al.,* 1995; *Bos and Spiers*, 2001; *Holdsworth*, 2004; *Gratier et al.,* 2011; *Massironi et al.,* 2011; *Torgersen and Viola*, 2014]. Since the characterization of weak faults has been mainly focused on major structures that accommodated significant displacement at the crustal scale. These studies implicitly suggest that fault weakness is a characteristic of mature fault zones.

Nonetheless, several studies highlighted that, in incipient stages of deformation, pressure solution and other processes lead to phyllosilicate segregation and reorganization, providing weak precursory horizon subsequently exploited by brittle faulting [e.g., *Alvarez et al.,* 1978; *Gratier and Gamond*, 1990; *Willemse et al.,* 1997; *Fagereng et al.,* 2010].

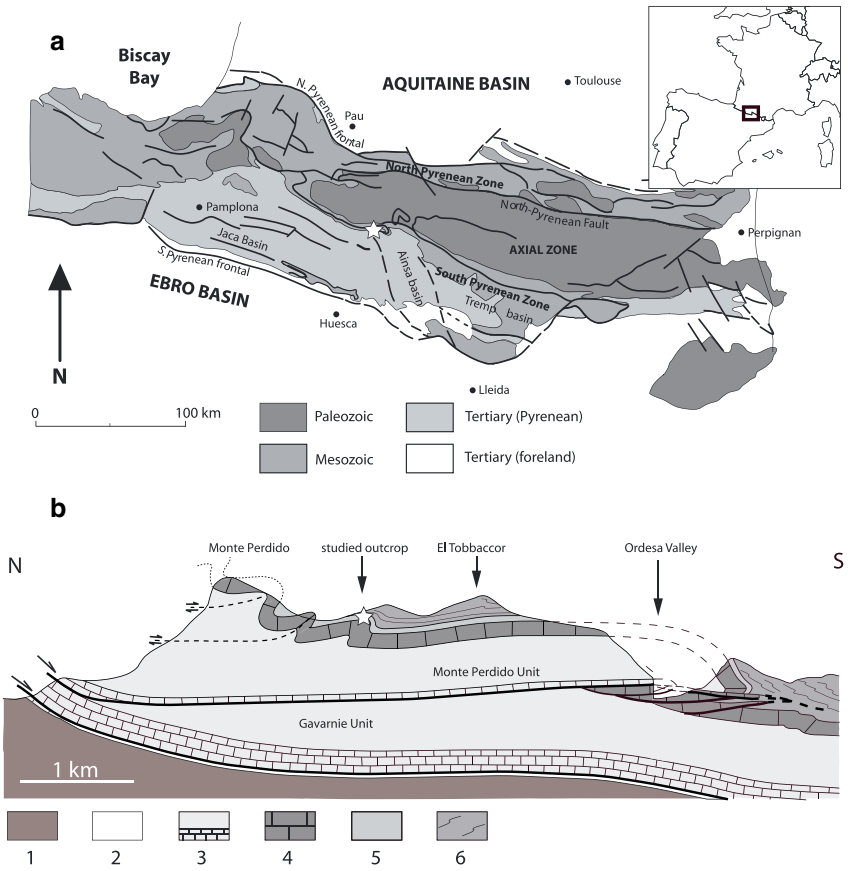

Figure 1. (a) Structural map of the Pyrenees. (b) Cross section of the Monte Perdido Massif modified from *Lacroix et al.* [2011]. 1. Paleozoic basement; 2. Triassic rock; 3. Cretaceous limestones and sandy limestones; 4. Paleocene-lower Ypresian limestones; 5. Lower Ypresian Millaris marls; 6. Ypresian Hecho Group turbidites.

However, an important and unanswered issue is how much deformation and alteration a fault zone has to experience before becoming "weak" and to provide an experimental constrain to this incipient weakness.

To address this topic, we performed a study of a low-displacement fault that formed in a detachment horizon: the Millaris thrust exposed south of the Monte Perdido Massif, southern Pyrenees of Spain (Figure 1) [*Lacroix et al.*, 2011]. We integrated field and microstructural analyses, with geochemical mass balances and with friction experiments of the Millaris fault rocks, in order to demonstrate significant fault weakening along an incipient fault.

2. Fault Zone Architecture and Deformation Mechanisms

The studied fault zone is located in the Monte Perdido unit belonging to the south Pyrenean thrust system (Figure 1). The activity of this fault zone is related to the emplacement of the Monte Perdido unit, and the associated folding occurred during the middle-late Lutetian to the late Bartonian [*Teixell,* 1996; *Remacha and Fernandez*, 2003].

The Millaris thrust is entirely developed within a 50 m thick homogeneous marly unit (lower Ypresian Millaris marls) that constitute both the hanging wall and the footwall of the studied fault [*Lacroix et al.,* 2011] (Figure 2).

The fault zone consists of a ~10 m thick, intensively foliated shear zone separated from the host marls by anastomosing and discontinuous shear surfaces that are mostly parallel to the bedding of the marls (Figures 2a and 2c). Outside the fault zone, the Millaris marls are affected by a more spaced north dipping regional cleavage (Figures 2c and 3a). The fault core is remarkably darker and richer in phyllosilicates than the marly protolith. Deformation resulted in the development of an oblique schistosity and synthetic C and C′ shear surfaces defining well-developed S-C(C′) tectonites [e.g., *Berthé et al.,* 1979; *Bos and Spiers*, 2001;

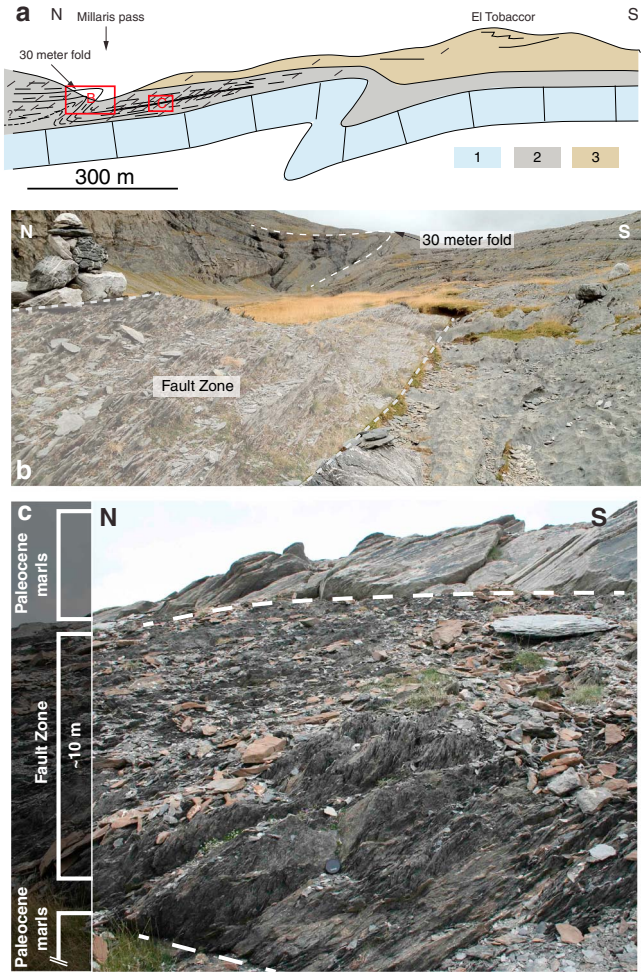

Figure 2. Field and structural observations in the Millaris fault. (a) Local cross section showing the spatial relationship between folds and the Millaris thrust fault (vertical scale = *X*). (b) Field photograph of the Millaris pass showing the structural relationship between the studied fault zone and folding. Note that the fault zone corresponds to a local décollement accommodating a 30 m wavelength fold developed in Millaris marls. (c) The Millaris fault corresponds to a top-to-the-south thrust fault developed in marly units (Millaris marls). Undeformed Millaris marls form both hanging wall and footwall feature slight pressure solution cleavage. Inside the fault zone ductile schistose and synthetic C and C′ shear surfaces are present. 1: Paleocene limestone; 2: Eocene Millaris marls; 3: Eocene turbidites.

Lacroix et al., 2011] (Figure 3b). Sigmoidal bodies in the tectonites are constituted by lenses of marly rock commonly folded and sutured along the S and C surfaces. S, C, and C′ surfaces show striations along the polished dark clay-rich surfaces and are sometimes decorated by millimeter-scale calcite slickenfibers suggesting that they all acted as localized and contemporaneous slipping planes.

The boundaries of the shear zone are underlined by tabular, centimeter- to decimeter-thick calcite shear veins affected by folding and microfaulting (Figure 3c). At the microscale, they are constituted by layered shear veins formed by incremental crack-seal opening parallel to the fault shear [*Lacroix et al.,* 2011] suggesting that part of the dissolved calcite reprecipitated right outside the fault core.

At the microscale, the regional cleavage affecting the host marls is represented by micron-scale pressure solution seams where calcite is slightly dissolved and along which detrital illite and chlorite (~5 μm long) are accumulated and reoriented (Figures 4a and 4b). In contrast, in the fault zone, the cleavage is defined by the alignment of thin crystallites of illite (<1 μm) and quartz grains (Figure 4c). The sigmoidal morphology of quartz grains and the cleavage is in agreement with the top-to-the south fault kinematics. Quartz grains inside the fault zone do not show any evidence of cataclasis, and quartz grain size is similar in both fault zone and host marls (Figure 4c). Their boundaries are sometimes corroded suggesting a local pressure solution of quartz (Figure 4c). Authigenic chlorite crystals are sporadically observed along shear surfaces where they define slickenfibres (Figure 4d). The preferred orientation of chlorite particles parallel to shear surfaces suggest that they crystallized contemporaneously to the shear movement (Figure 4d).

Even if we cannot exclude the presence of a more clay-rich horizon within the marls facilitating the fault nucleation, the development of oblique shear surfaces with respect to the stratigraphy inside the fault zone suggests that the high concentration of illite and chlorite minerals is due to fault-related deformation rather that an inherited stratigraphic level (Figure 2c and details in section 4).

All these observations suggest that deformation inside the fault zone involved both pressure solution and frictional sliding along both the foliation and synthetic shear surfaces that are coated by illite and chlorite (Figures 4c and 4d).

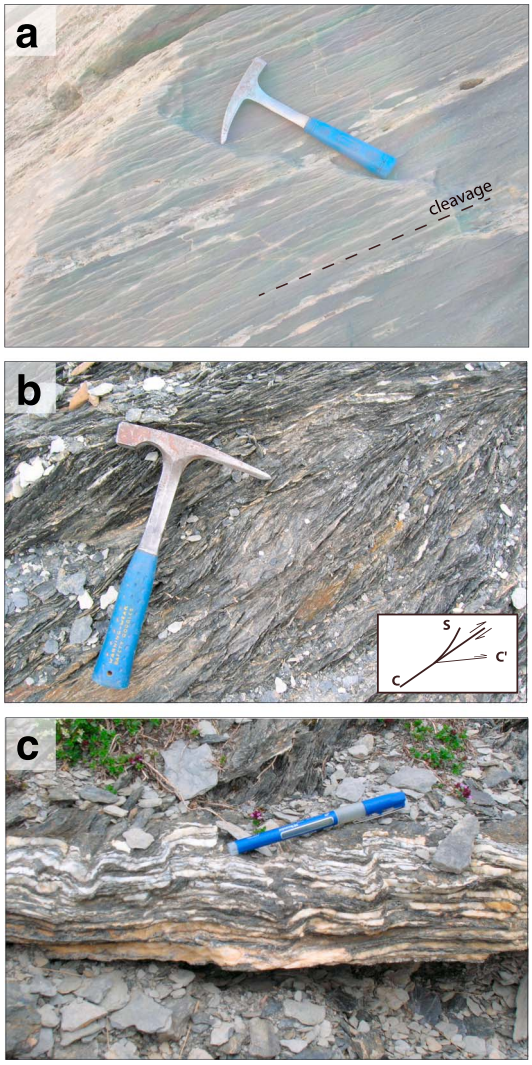

Figure 3. Field photographs illustrating the deformation in the Millaris fault zone. (a) Parent marl protolith from the hanging wall. Note the presence of the spaced pressure solution cleavage. (b) Detail of the fault zone featuring C-C'-S fabrics indicating a displacement toward the south. (c) Centimeter-thick calcite tabular shear vein along the fault boundary.

Field observations show that the Millaris fault has a limited along-strike continuity of a few hundred meters and represents the detachment level of a fault-propagation fold with a ~30 m wavelength overturned fold (Figures 2a and 2b). Both evidences suggest that the fault accommodated a limited displacement of a few tens of meters. Even lacking reliable displacement markers inside the fault zone, it is possible to appreciate significant variations in the foliation intensity (Figure 5a), implying a nonhomogeneous strain partitioning along several shear bands.

3. Analytical and Experimental Methods

Field and microstructural work have been used to define key localities to collect rock samples that we used to characterize rock chemistry, possible volume loss, temperature, and frictional properties of the fault during deformation. Samples were collected along a selected vertical transect across the fault zone (Figure 5a). Host marls were also collected several meters from fault (Figure 5a).

3.1. Rock Chemistry and Chemical Mass Transfer Calculations

We determined the bulk rock chemistry of five representative samples from the host marls and eight from the fault zone (Figure 3a and details in Table 1) that were analyzed for major elements. Analyses were performed on molten samples using a Philips PW2400 X-ray Fluorescence Spectrometer equipped with a rhodium anode (University of Lausanne). Subsequently, we evaluated the chemical mass transfers between the fault zone and parent marls using the statistical Isocon method of *Baumgartner and Olsen* [1995]. The bulk rock chemical composition of the protolith (0) has been calculated averaging the four intact marls compositions. The related 1σ standard deviation highlights the initial chemical heterogeneities and is used as error in the mass balance calculations. Eight bulk rock chemical compositions of samples from the fault zone (A) have been used to estimate mass and volume changes in the fault zone compared to the protolith. All bulk chemical compositions and measured skeletal densities of samples are presented in Table 1.

During the Isocon mass transfer calculations, immobile chemical components (i) are statistically selected by an algorithm that identifies the maximum number of chemical components that are compatible, within their 1σ uncertainties, with a same isocon. Thus, the isocon line is defined by the equation:

$$\log C_i^A = \log\left(\frac{M^0}{M_A}\right) + \log C_i^0 \quad (1)$$

Mass transfers for all chemical components are estimated from the isocon line, and results of the calculations are portrayed in log-log isocon diagrams (Figure 6). Major element concentrations and mass changes are

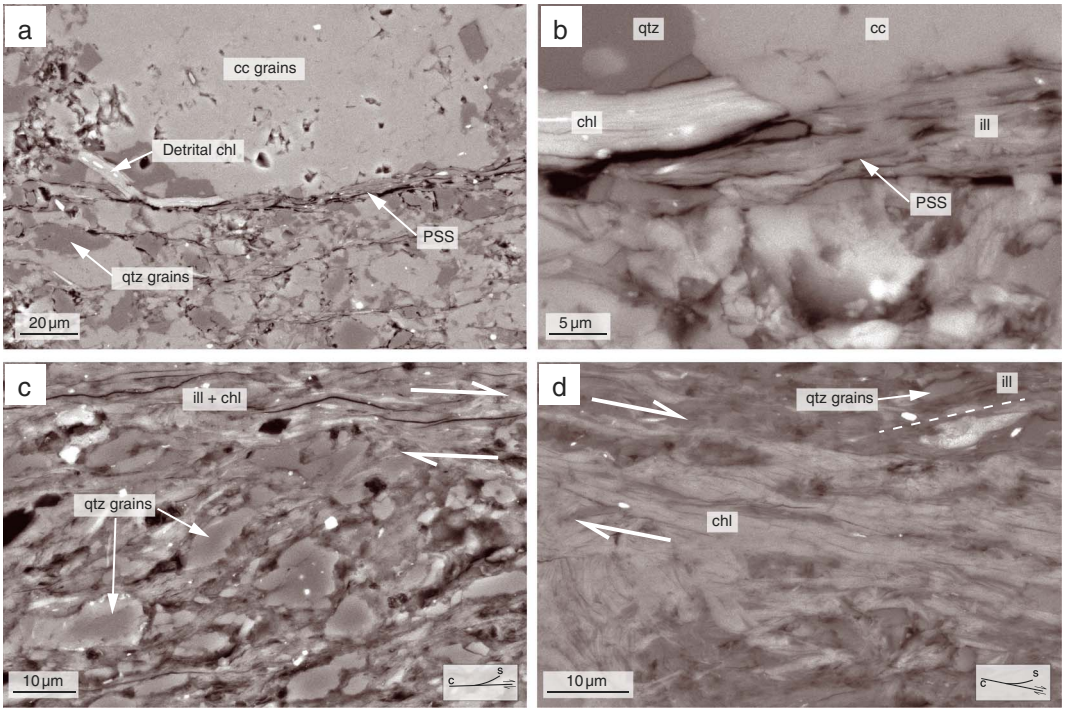

Figure 4. Backscattered scanning electron (BSE) images illustrating the deformation in the parent marls and fault zone. (a) Pressure solution surfaces in the parent marls. Cleavage is underlined by detrital chlorite and illite grains. (b) Inset of Figure 4a. (c) Morphology of the cleavage from the fault zone. The cleavage is defined by the alignment of small illite crystals and quartz grains, which define sigmoid cleavage. Note the absence of calcite compared to parent marls. (d) Example of authigenic chlorite coating the shear surfaces. The preferential orientation of chlorite parallel to shear surface argues that chlorite precipitated contemporaneously to shear movement.

expressed in g/100 g of the initial rock (i.e., the protolith), while density and related volume changes are expressed in percent (Table 2).

3.2. Deformation Temperature Estimations

In order to constrain temperature conditions in the fault zone, we analyzed the chemical composition (Si, Fe, Mg, Al, Ti, K, Ca, and Na) of authigenic chlorite. Chlorite chemistry was determined at the University of Lausanne using a JEOL model 8200 superprobe electron microprobe equipped with five wavelength-dispersive spectrometers (WDS) with LIF, PET, TAP, LDE1, and LDE2 crystals. The microprobe operated with a 20 kV tension, a 10 nA current intensity, and a 3 µm beam diameter. The used standards are wollastonite (Si, Ca), hematite (Fe), olivine (Mg), andalusite (Al), TiO_2 (Ti), orthoclase (K), and albite (Na). Temperature of authigenic chlorite was calculated using the chlorite composition model [*Vidal et al.,* 2005] with a pure water activity aH2O and a pressure of 1 kbar (Table 3).

An independent estimate of the maximum temperature during faulting was provided by Raman spectrometry on carbonaceous material (RSCM) [*Lahfid et al.,* 2010]. RSCM was performed on two samples from the fault zone (samples Mi07-06 and Mi07-08) and on one sample of host marls located at ~200 m below the fault zone in order to avoid any potential influence of shear heating and hydrothermal circulation on the temperature. Using a Renishaw inVia Reflex system, 10–15 spectra were obtained at the Bureau de Recherches Géologiques et Minières (France) on polished thin sections with a 100X objective (numerical aperture = 0.9) of DM2500 Leica microscope. The Raman scattering was excited by 514 nm wavelength of an argon-ion laser with a power of around 0.5 mW at sample surface. After elimination of the Rayleigh diffusion by edge filters, the Raman signal was first dispersed using 1800 lines/mm and then analyzed by a deep depletion CCD detector (1024 × 256 pixel). Before each session of measurements, the spectrometer was calibrated using the 520.5 cm^{-1} line of a silicon standard. The Raman spectrometer was operated using continuous scanning mode with large spectral

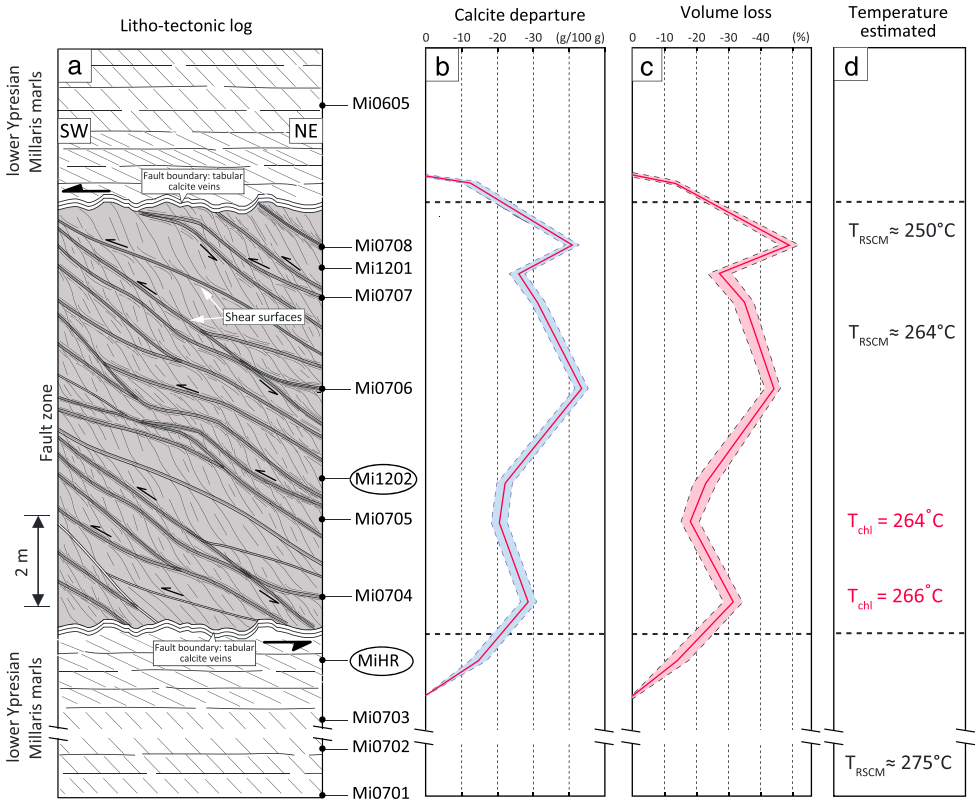

Figure 5. Multiproxy physicochemical parameters of the Millaris fault. (a) Schematic lithotectonic log of the fault outcrop with samples locations (modified from *Lacroix et al.* [2011]). (b) Calcite departure calculated using the Isocon statistical approach [*Baumgartner and Olsen,* 1995]. Calcite loss is given in g/100 g. (c) Calculated volume loss in the fault zone. (d) Temperature estimated with the chlorite composition thermometer of *Vidal et al.* [2006] and Raman spectrometry on carbonaceous material (RSCM) thermometer of *Lahfid et al.* [2010].

windows from 700 to 2000 cm^{-1}, which include all the first-order bands, and allows defining properly the baseline. In order to avoid analytical mismatches, we followed the procedures and spectra analysis described in *Lahfid et al.* [2010].

3.5. Friction Experiments

To test the strength of the Millaris fault rock and associated host rocks, a suite of 15 friction experiments were conducted on a biaxial rock deformation apparatus [*Collettini et al.,* 2014] hosted in the High Pressure-High Temperature Laboratory of Istituto Nazionale di Geofisica e Vulcanologia, Rome. All the experiments were performed on pieces of intact rocks (wafers) in order to reshear the natural fabrics in the in situ geometry and at pressure conditions representative of the estimated burial depths of the fault during its activity.

During each experiment, two identical wafers of the same sample were sheared in a double-direct shear configuration [e.g., *Collettini et al.,* 2009] at constant normal stress (10, 15, 20, 30, 40, and 50 MPa) at room temperature and under water-saturated conditions. Using this configuration, the normal stress σ_n and the shear stress τ were applied perpendicular and parallel to the natural C shear foliation, respectively.

Samples were sheared at 10 μm/s sliding velocity until reaching the steady state dynamic friction, and then we imposed velocity steps (1 to 300 μm/s) and slide-hold-slide sequences (3–1000 s) to assess the frictional stability and healing properties of the samples in the framework of the *rate-state friction* theory [e.g., *Marone*, 1998]. Residual shear stress at steady state was measured at each normal stress.

In addition, we performed two experiments at 30 MPa normal stress and 1 μm/s sliding velocity that were halted soon after reaching the steady state friction. These experiments were designed to recover samples for detailed microstructural analysis.

Table 1. Bulk Chemical Compositions of the Eight Samples Representative for the Chemical Evolution Throughout the Millaris Thrust and Mean Composition of Undeformed Marls ($n = 4$)

Protolith			Damage Zone	Deformed Sediment						
			Mi-HR	Mi07-04	Mi07-05	Mi07-06	Mi07-07	Mi07-08	Mi12-01	Mi12-02
n = 4 *density*	*2.61*		*2.55*	*2.57*	*2.53*	*2.6*	*2.61*	*2.57*	*2.55*	*2.55*
wt %		1σ								
SiO_2	27.79	1.43	33.51	38.85	35.19	52.14	41.45	45.49	36.34	34.96
TiO_2	0.34	0.02	0.42	0.43	0.42	0.58	0.46	0.65	0.48	0.43
Al_2O3_3	8.33	0.47	9.81	12.03	11.23	15.85	12.54	17.56	12.30	11.52
Fe_2O3_3	2.80	0.36	3.36	4.16	3.61	4.03	3.94	5.31	4.03	4.00
MnO	0.06	0.01	0.05	0.05	0.05	0.03	0.05	0.04	0.06	0.06
MgO	1.70	0.36	1.74	1.72	1.58	1.73	1.64	2.16	1.80	1.77
CaO	30.13	0.91	25.85	19.90	23.07	9.39	18.44	13.25	21.64	23.04
Na_2O	0.30	0.02	0.58	0.21	0.56	0.49	0.20	0.45	0.55	0.39
K_2O	1.60	0.06	1.91	2.38	2.01	3.35	2.49	3.61	2.30	2.21
P_2O_5	0.07	0.00	0.08	0.06	0.07	0.09	0.07	0.10	0.08	0.06
LOI	26.23	0.78	22.70	19.28	21.44	11.63	18.09	10.53	20.04	21.11
Cr_2O_3	0.01	0.00	0.01	0.02	0.02	0.02	0.01	0.02	0.02	0.02
NiO	0.00	0.00	0.01	0.01	0.01	0.01	0.01	0.01	0.01	0.01
Total	99.37	0.11	100.01	99.10	99.26	99.33	99.38	99.18	99.65	99.58

4. Results

4.1. Mass Transfer Across the Fault Zone

The Millaris fault composes an ideal candidate for mass balance because (1) the mineralogy is the same in host sediments and fault zone (with nonetheless variation of mineralogical proportions related to the deformation) and (2) parent marls compositions are chemically homogeneous with a low standard deviation (1σ) (Table 1). The results of chemical mass balance are illustrated in Table 2 and Figure 5. They show that the most mobile chemical components in the fault zone are CaO and the related CO_2 (measured as the major constituent of the L.O.I., see Table 2 and Figure 7a). The losses of CaO vary from 12.01 to 25.06 g/100 g with a higher CaO loss calculated for samples from more deformed shear surfaces (Mi0704, Mi0706, and Mi0708, Figures 5a and 7a). Carbonates in fault zone and host sediment mainly consist of pure calcite with a composition of $(Ca_{0.98}Mg_{0.01}Fe_{0.01})CO_3$. Considering a pure calcite composition ($CaCO_3$), the absolute losses of calcite in the fault zone compared to the undeformed marls protolith vary between 21.4 and 44.7 g for 100 g of initial rock (Figures 5b and 7a). Because no significant density variations between the undeformed protolith and the fault zone have been noticed (most of the

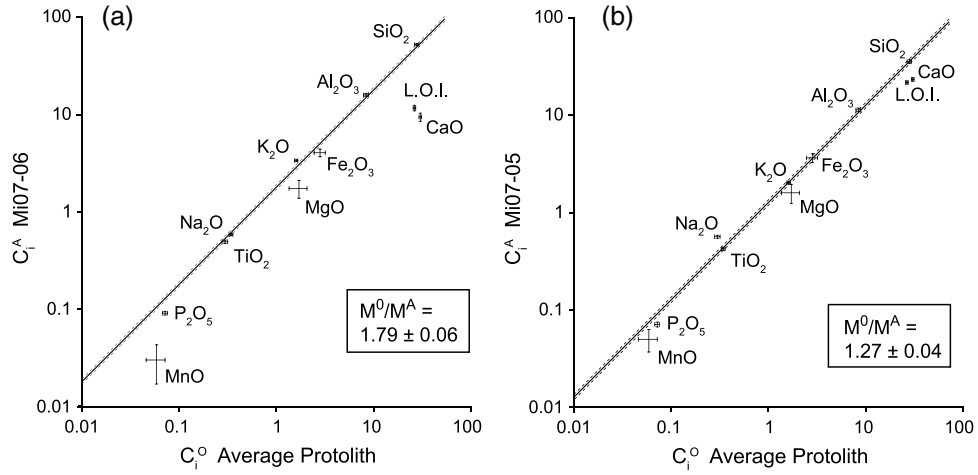

Figure 6. Mass balance diagram from the log-log Isocon method [*Baumgartner and Olsen*, 1995] illustrating results of mass transfers between the parent Millaris marls and deformed fault rocks with different shear strain. (a) Example of the sample Mi07-05 which consists to a S-C(C') tectonites. (b) Example of sample Mi07-06 affected by to a high shear strain.

Table 2. Result of the Mass Balances Calculations (Estimated With the Statistical Isocon Method From *Baumgartner and Olsen* [1995]) Between the Marls Protolith and the Altered Samples in the Millaris Fault Zone[a]

Sample	Mi-HR		Mi07-05		Mi12-02		Mi12-01		Mi07-04		Mi07-07		Mi07-08		Mi07-06	
	Value	1σ	Value	1σ	Value	1σ	Value	1σ	Value	1σ	Value	1σ	Value	1σ	Value	1σ
M^0/M^A	1.19	0.04	1.27	0.04	1.32	0.04	1.41	0.04	1.46	0.05	1.52	0.05	1.99	0.08	1.79	0.06
$\chi 2$	0.50		2.06		3.73		2.98		0.66		0.63		1.64		3.45	
$\chi 2/(n-1)$	0.10		0.41		0.53		0.60		0.22		0.21		0.82		1.15	
Q	0.97		0.73		0.71		0.56		0.72		0.73		0.20		0.18	
ni/11	6		6		8		6		4		4		3		4	
Mass change (g 100 g^{-1})	−16.17	2.50	−21.18	2.31	−24.42	2.04	−28.86	2.00	−31.49	2.22	−34.33	2.10	−49.76	1.93	−44.24	1.71
Density change (%)	−2.30	0.78	−3.07	0.79	−2.30	0.78	−2.30	0.78	−1.53	0.78	0.00	0.77	−1.53	0.78	−0.38	0.77
Volume change (%)	−14.19	16.65	−18.69	15.74	−22.64	14.48	−27.19	13.83	−30.43	13.98	−34.33	13.08	−48.98	10.99	−44.02	10.97
Absolute mass change	Value	1σ	Value	1σ	Value	1σ	Value	1σ	Value	1σ	Value	1σ	Value	1σ	Value	1σ
SiO_2	0.12	2.06	−0.02	2.01	−1.43	1.94	−2.02	1.91	−1.11	1.96	−0.58	1.94	−4.92	1.84	1.31	1.88
Al_2O_3	−0.16	0.66	0.54	0.65	0.37	0.63	0.41	0.63	−0.06	0.63	−0.09	0.62	0.52	0.63	0.52	0.60
Fe_2O_3	−0.01	0.48	0.04	0.47	0.21	0.47	0.06	0.46	0.05	0.45	−0.22	0.45	−0.13	0.42	−0.56	0.43
MnO	−0.02	0.02	−0.02	0.02	−0.01	0.02	−0.02	0.02	−0.02	0.02	−0.03	0.02	−0.04	0.01	−0.04	0.02
MgO	−0.26	0.47	−0.46	0.46	−0.37	0.45	−0.43	0.44	−0.52	0.44	−0.63	0.43	−0.62	0.40	−0.74	0.41
CaO	**−8.66**	**1.35**	**−12.01**	**1.28**	**−12.84**	**1.24**	**−14.88**	**1.20**	**−16.57**	**1.20**	**−18.14**	**1.16**	**−23.62**	**1.06**	**−25.06**	**1.06**
Na_2O	0.19	0.03	0.15	0.03	−0.01	0.03	0.10	0.03	−0.15	0.02	−0.17	0.02	−0.07	0.02	−0.02	0.02
K_2O	−0.01	0.10	−0.01	0.09	0.07	0.09	0.04	0.09	0.04	0.09	0.04	0.09	0.22	0.10	0.27	0.09
TiO_2	0.01	0.02	−0.01	0.02	−0.01	0.02	0.00	0.02	−0.05	0.02	−0.04	0.02	−0.01	0.02	−0.02	0.02
P_2O_5	−0.01	0.01	−0.02	0.01	−0.02	0.01	−0.02	0.01	−0.03	0.01	−0.03	0.01	−0.02	0.01	−0.02	0.00
L.O.I.[b]	−7.37	1.17	−9.37	1.12	−10.37	1.08	−12.09	1.05	−13.07	1.05	−14.45	1.02	−21.06	0.91	−19.87	0.92
CO_2 in $CaCO_3$	−6.79	1.06	−9.42	1.01	−10.07	0.97	−11.67	0.94	−13.00	0.94	−14.24	0.91	−18.53	0.83	−19.67	0.83
$CaCO_3$ recalculated	−15.45	2.42	−21.43	2.29	−22.91	2.21	−26.55	2.14	−29.57	2.13	−32.38	2.07	−42.15	1.88	−44.72	1.89
L.O.I. recalculated	−0.58	0.11	0.05	0.11	−0.30	0.11	−0.42	0.10	−0.06	0.11	−0.21	0.11	−2.53	0.08	−0.20	0.09

[a] M^0/M^A is value of the slope of the isocon. The number of elements compatible with the isocon is ni. Absolute mass change is expressed in g/100 g. nCaO = $n$$CO_2$. $CaCO_3$ = CaO + CO_2. Density and volume changes are expressed in percent. Samples are classified as a function of the increase of the CaO loss. Note that the CaO (boldface) is the most mobile component.
[b] L.O.I., Lost on Ignition.

Table 3. Mineral Formulas of the Present Minerals and Results From the Normative Mineral Distribution

Mineral Formulas Used for Modal Calculation

Apatite	$Ca_5(PO_4)_3(OH)$
Illite	$(Al_{1.83}Fe_{0.09}Mg_{0.11})[Si_{3.10}Al_{0.88}Ti_{0.02}O_{10}](K_{0.86}Na_{0.11}Ca_{0.01})(OH)_2$
Chlorite	$(Mg_{1.79}Fe_{2.37}Al_{1.61}\square_{0.23})(Si_{2.74}Al_{1.26})O_{10}(OH)_8$
Albite	$Na[AlSi_3O_8]$
Rutile	TiO_2
Pyrite	FeS_2
Quartz	SiO_2
Calcite	$CaCO_3$

	Protolith	*Mi12-HR*	*Mi07-05*	*Mi012-02*	*Mi012-01*	*Mi07-04*	*Mi07-07*	*Mi07-08*	*Mi07-06*
Apatite	0.15	0.16	0.15	0.13	0.16	0.12	0.14	0.20	0.18
Illite	15.87	18.76	19.60	21.73	22.37	24.31	24.49	33.89	32.72
Chlorite	12.28	13.92	18.41	16.73	18.61	12.72	17.00	21.16	18.63
Albite	0.00	0.00	0.00	0.00	0.00	0.08	0.00	0.00	0.00
Rutile	0.39	0.48	0.48	0.48	0.54	0.50	0.50	0.68	0.63
Pyrite	0.00	0.00	0.00	0.00	0.00	0.00	0.00	0.00	0.00
Quartz	17.33	20.94	20.81	20.21	20.46	25.60	25.33	21.86	31.48
Calcite	53.97	45.74	40.56	40.72	37.86	36.67	32.55	22.21	16.36
Quartz relative mobility		4.07	−11.09	−14.64	−18.94	12.24	−0.85	−35.49	−0.42
Calcite relative mobility		−14.57	−23.93	−24.17	−27.97	−26.11	−31.89	−42.61	−45.01

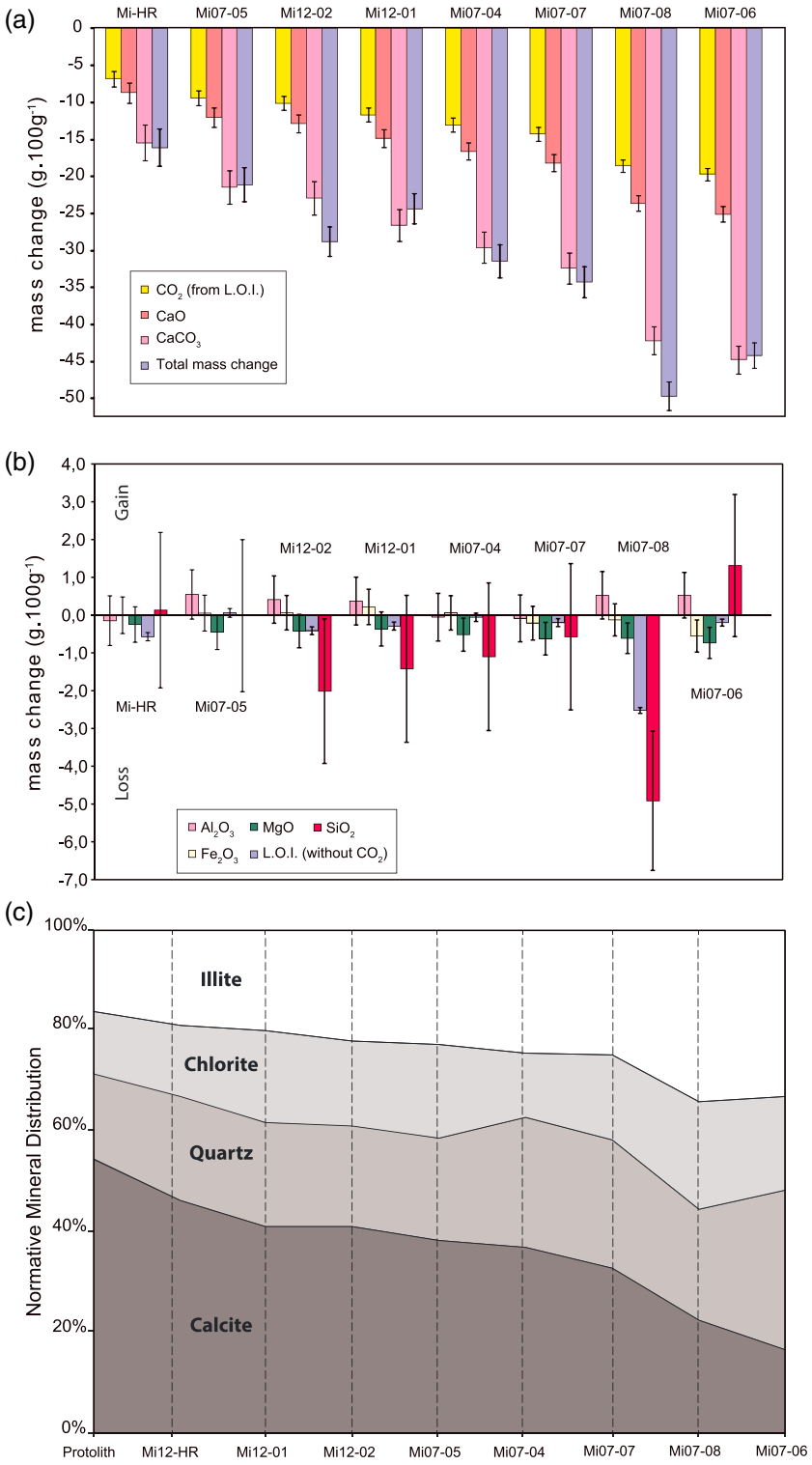

Figure 7. Absolute mass change given in g 100 g^{-1} for (a) Cao, CO_2, and $CaCO_3$ and for (b) Al_2O_3, MgO, SiO_2, and Fe_2O_3. (c) Normative composition of the major mineral phases present.

minerals having the same density; Table 1), we infer that calcite departure directly induces volume loss. Such calcite departure represents a volume reduction from 20 to 50% in the fault zone compared to the undeformed marls (Figure 5c and Table 2). On the basis of widespread field and microstructural evidence, the calcite departure is most likely driven by effective pressure solution creep.

Table 4. Chlorite Chemical Composition and Temperature Estimations Calculated Using the Thermodynamic Model Developed by *Vidal et al.* [2005][a]

	Mi07-04							Mi07-05											
Number	3	7	14	22	25	27	28	34	35	39	40	43	45	52	53	56	58	59	66
SiO_2	25.6	25.5	25.6	25.4	25.9	26.2	27.2	25.4	26.2	26.0	25.9	25.7	25.5	25.7	25.6	25.5	25.8	25.9	26.6
TiO_2	0.0	0.0	0.0	0.0	0.0	0.0	0.0	0.0	0.0	0.0	0.0	0.0	0.0	0.0	0.0	0.0	0.0	0.1	0.0
Al_2O_3	22.5	22.7	22.7	22.6	22.7	23.2	23.5	23.1	23.0	23.5	23.4	22.3	23.0	22.4	22.4	23.0	22.5	22.8	23.9
FeO	26.6	27.0	26.0	27.1	25.4	26.7	24.6	27.3	26.2	26.9	25.6	26.1	26.0	26.3	27.4	27.7	27.0	27.1	25.9
MnO	0.0	0.0	0.0	0.0	0.0	0.0	0.0	0.0	0.0	0.0	0.0	0.0	0.0	0.0	0.0	0.0	0.0	0.0	0.0
MgO	11.8	11.6	12.1	10.9	12.0	11.5	11.4	10.7	11.5	11.1	11.2	11.8	10.8	11.2	10.7	10.8	11.6	10.9	11.1
CaO	0.2	0.3	0.5	0.4	0.5	0.1	0.2	0.3	0.3	0.3	0.5	0.4	0.9	0.9	0.3	0.3	0.2	0.2	0.2
Na_2O	0.1	0.0	0.1	0.0	0.0	0.0	0.1	0.0	0.0	0.0	0.0	0.0	0.0	0.0	0.0	0.0	0.0	0.0	0.0
K_2O	0.0	0.1	0.1	0.1	0.1	0.1	0.1	0.0	0.0	0.1	0.0	0.0	0.0	0.0	0.0	0.0	0.0	0.0	0.0
14 oxygen																			
Si	2.7	2.7	2.7	2.7	2.7	2.8	2.8	2.7	2.8	2.7	2.8	2.8	2.7	2.7	2.8	2.7	2.7	2.8	2.8
Al	2.8	2.8	2.9	2.8	2.9	2.8	2.9	2.9	2.9	2.9	2.9	2.8	2.9	2.8	2.8	2.9	2.8	2.9	2.9
Al^{IV}	1.3	1.3	1.3	1.3	1.3	1.2	1.2	1.3	1.2	1.3	1.2	1.2	1.3	1.3	1.2	1.3	1.3	1.2	1.2
Al^{VI}	1.5	1.6	1.6	1.6	1.6	1.6	1.6	1.6	1.6	1.7	1.7	1.6	1.6	1.6	1.6	1.6	1.6	1.6	1.7
Fe	2.4	2.4	2.4	2.3	2.4	2.3	2.4	2.4	2.3	2.4	2.3	2.3	2.3	2.4	2.5	2.5	2.4	2.4	2.3
Mg	1.8	1.9	1.8	1.9	1.7	1.9	1.8	1.7	1.8	1.7	1.8	1.9	1.7	1.8	1.7	1.7	1.8	1.7	1.7
Mn	0.0	0.0	0.0	0.0	0.0	0.0	0.0	0.0	0.0	0.0	0.0	0.0	0.0	0.0	0.0	0.0	0.0	0.0	0.0
K	0.0	0.0	0.0	0.0	0.0	0.0	0.0	0.0	0.0	0.0	0.0	0.0	0.0	0.0	0.0	0.0	0.0	0.0	0.0
Na	0.0	0.0	0.0	0.0	0.0	0.0	0.0	0.0	0.0	0.0	0.0	0.0	0.0	0.0	0.0	0.0	0.0	0.0	0.0
Ca	0.0	0.0	0.0	0.1	0.0	0.1	0.0	0.0	0.0	0.0	0.1	0.1	0.1	0.1	0.0	0.0	0.0	0.0	0.0
Ti	0.0	0.0	0.0	0.0	0.0	0.0	0.0	0.0	0.0	0.0	0.0	0.0	0.0	0.0	0.0	0.0	0.0	0.0	0.0
X_{Fe}	0.6	0.6	0.6	0.5	0.6	0.5	0.6	0.6	0.6	0.6	0.6	0.6	0.6	0.6	0.6	0.6	0.6	0.6	0.6
T°C Vidal	**282**	**293**	**292**	**280**	**264**	**259**	**195**	**279**	**252**	**269**	**257**	**270**	**265**	**269**	**261**	**284**	**272**	**258**	**238**

[a]Boldface line: Temperature calculated using the thermodynamical model of *Vidal et al.* [2006].

Conversely, the SiO_2 chemical component shows more limited variations ranging from +1.31 to −4.92 g for 100 g of host rock, all within the error ranges except for sample Mi0708 (Table 2 and Figure 7b). This oxide is partitioned between quartz, illite, and chlorite. In phyllosilicates SiO_2 is associated with FeO, Al_2O_3, and K_2O, which do not show significant variations (Figure 7b).

To evaluate the mobility of mineral species during deformation, we reconstructed the normative mineral composition of the host and fault rocks from the bulk chemical composition, knowing the mineral phases present in the samples and their compositions (Table 3). The minerals present were identified by XRD analysis and the chemical composition of calcite, chlorite, and illite were measured by microprobe. The calculated normative mineral assemblages of all samples are presented in Figure 7c and Table 3.

The relative mass change of quartz is calculated using the passive concentration of insoluble minerals in the fault zone compared with the parent marls as [*Gratier et al.*, 2013]

$$\frac{\Delta M}{M_0} = \left(\frac{I_p}{I_e}\right) \cdot \left(\frac{S_e}{S_p}\right) - 1 \quad (2)$$

where I_p and I_e are the content in insoluble minerals (mainly chlorite and illite) in the fault zone and parent marls, respectively, and S_e and S_p correspond to the modal proportion of quartz in fault zone and protolith, respectively. The relative mass change of quartz varies between +12% and −35% of the initial content in the parent rocks (Table 3). However, quartz composes ~17% of the total parent rock mineral composition, and therefore, the relative mass change represents only 2.1% to −6.0% of the total mass change. In comparison, calcite represents between −15.5% and −44.7% of the total mass change. As a consequence, quartz may be considered as relatively immobile compared to $CaCO_3$ (see discussion in section 5).

The variations of the other oxides during the shearing event are thus considered insignificant compared to the $CaCO_3$ loss and are thought to have no direct impact on the volume variations and over the rheology of the fault zone.

4.2. Temperature Estimations

The chemical compositions of synkinematic chlorite crystallized along the shear surfaces of the fault zone (samples Mi07-04 and Mi07-05; Table 4) are similar. They consist to ferromagnesian chlorite with

Table 5. Raman Spectrometry Data of Carbonaceous Material From the Millaris Fault Zone Area[a]

Sample	Description	Distance From the Top of FZ	RA1 Parameter Mean	SD	Temperature (°C)	SD
Mi07-01	FW	25 m	0.60	0.03	275	27
Mi07-07	FZ	1 m	0.59	0.01	264	9
Mi07-08	FZ	0.5 m	0.58	0.01	250	20
MP11-01	FW	>100 m	0.57	0.01	250	10

[a]RA1: Peak ratio after *Lahfid et al.* [2010]. Temperatures are calculated according to the procedure described by *Lahfid et al.* [2010]. FZ: Fault Zone; FW: Footwall.

Fe/(Fe + Mg) ratios ranging between 0.56 and 0.59 (Table 4) and can be expressed as the activities of the end-members determined by *Vidal et al.* [2001]. Therefore, the temperature of chlorite formation has been determined using the thermodynamic thermometers form *Vidal et al.* [2005, 2006]. Calculated temperatures vary between 238°C and 293°C, with a mean value of 264 ± 20°C (Figure 5d and Table 4).

Peak temperature estimated via RSCM for the three samples inside and outside the fault zone cluster between 250°C and 275°C, with a mean temperature of 262 ± 12°C (Table 5). The sample collected at 200 m below the fault zone (MP11-01) give a temperature of about 260°C.

Both thermometers used in this study independently indicate a similar peak temperature of about ~260°C for all analyzed samples. The same temperature recorded in both synkinematic deformation within the fault zone and the undeformed protolith suggests that frictional heating produced during the fault-related deformation was relatively low and/or short lived. Considering the regional paleogeothermal gradient of 34°C/km estimated by *Lacroix et al.* [2012], the deformation depth was about 7 km.

4.3. Mechanical Properties of Fault Rocks

The steady state shear resistance, τ, of samples from the host marls and the Millaris fault rocks is in a linear relationship with the applied normal stress σ_n, consistently with a Mohr-Coulomb-type failure envelope, with the slope of the line representing the average friction (Figure 8a). Wafers from the Millaris parent marls show a coefficient of friction $\mu = 0.39$ that is significantly lower than that of average crustal rocks and of surrounding rocks composed of massive limestone and dolostone $\mu = 0.6$–0.85 [*Byerlee*, 1978; *Scuderi et al.,* 2013]. We note that samples of the host marls were collected close to the fault zone and they show a slightly more intense pressure solution cleavage with respect to the undisturbed Millaris marls. As a consequence, the coefficient of friction we measured on intact marls can be considered a lower bound of the host rock frictional strength. Fault rocks of the Millaris thrust show even lower friction, $\mu = 0.27$ (Figure 8a), indicating that slip is energetically favored within the fault zone.

Fault weakness is justified by the sliding during the experiments along the preexisting foliation. This fabric is composed of illite and chlorite horizons (respectively, C, C′, and S planes; see *Lacroix et al.* [2011] for detailed description) that form an interconnected fabric between strong calcite-rich residual lithons (Figure 4c).

Velocity step tests modeled with a Dieterich-type *rate-state* equation [*Dieterich*, 1972] yield positive (*a-b*) parameters (Figure 8b) suggesting that frictional sliding along clays was potentially associated to aseismic creep of the Millaris thrust, in agreement with previous studies on phyllosilicate-rich rocks [e.g., *Collettini et al.,* 2011; *Lockner et al.,* 2011; *Carpenter et al.,* 2011; *Ikari and Saffer,* 2011; *Tesei et al.,* 2014].

Slide-hold-slide tests were performed to evaluate the potential fault restrengthening. We used a background sliding velocity of 10 μm/s alternating with hold periods of 3–1000 s. Peak strength upon reshearing, $\Delta\mu$, is usually observed to linearly increase with $\log_{10}$(time) [*Dieterich*, 1972; *Marone*, 1998], and healing rates can be calculated as

$$\beta = \Delta\mu / \log_{10}(t) \tag{3}$$

Our data show low healing rates of Millaris fault zone materials with respect to pure calcite fault gouge (Figure 8b). Moreover, a significant divergence in healing behavior is observed between fault rocks and parent marls: the Millaris marls show a high restrengthening ($\beta_{max} = 0.0071$) whereas fault rocks show negligible recovery of strength ($\beta_{max} = 0.0008$, Figure 8b). Near-zero restrengthening suggests that the fault zone does not accumulate elastic energy during quasi-static periods, thus promoting aseismic creep [*Tesei et al.,* 2012]. Microstructural studies of sheared samples confirm that sliding surfaces activated

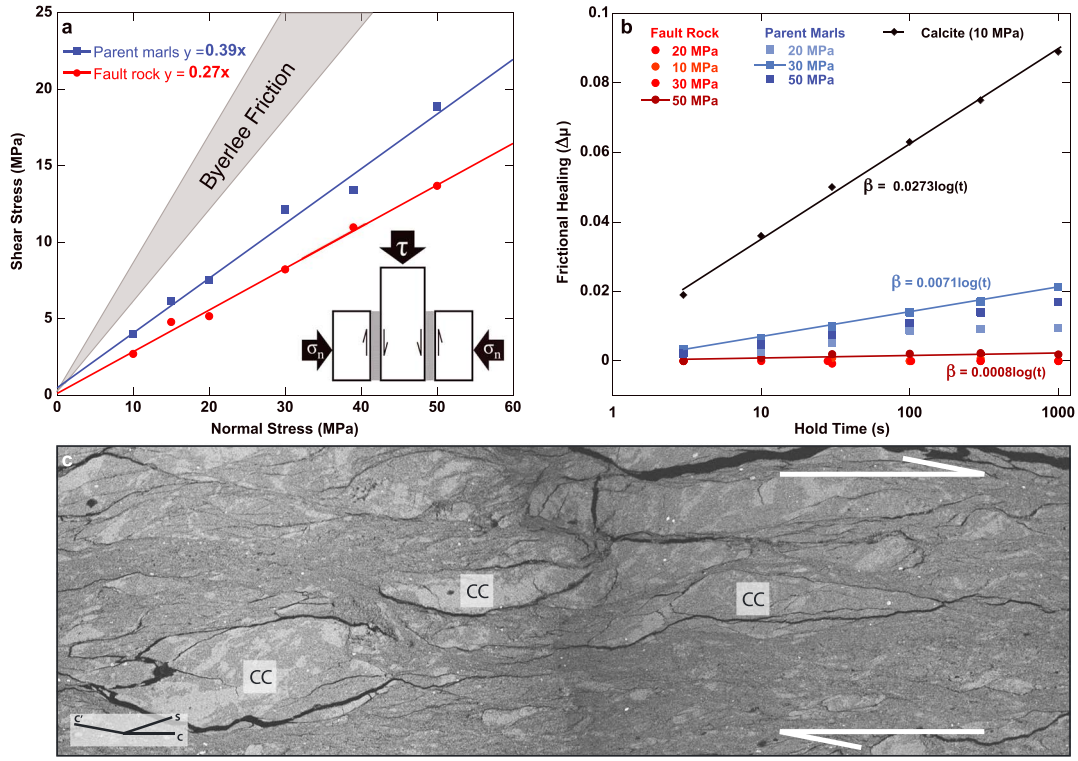

Figure 8. Friction experiments on intact wafers. (a) Steady state shear stress as a function of normal stress measured during stable sliding. The slope of the fit lines represents the average dynamic friction μ. The parent marls and the fault rocks display low frictional strength $\mu = 0.39$ and $\mu = 0.27$, respectively; Byerlee friction range ($\mu = 0.6$–0.85) is shown for comparison. Inset shows the double-direct experimental configuration where three steel blocks shear identical layers of a sample. (b) Frictional healing ($\Delta\mu$) as function of hold time for experiments conducted at 10 (only for fault rock), 20, 30, and 50 MPa for both fault core and host marls. The healing rate is $\beta = \Delta\mu/\log_{10}(t)$. Fault core rocks show no restrengthening after slip whereas host marls demonstrate high healing rate. Healing of pure calcite is shown for comparison (T. Tesei, unpublished data, 2013). (c) SEM-BSE image of the experimentally sheared fault rock sample Mi12-01. The total shear displacement is ~25 mm, and the steady state friction $\mu = 0.27$. Fissuring occurs along the experimentally gliding S-C(C') foliation between undeformed calcite-rich residual clasts. CC: calcite-rich residual clast.

during the experiments are localized along the preexisting phyllosilicate-rich foliation (Figure 8c). Within the experimental samples, hard, sigmoidal, calcite-rich clasts lie undeformed within the phyllosilicate network that is fissured along phyllosilicate-rich slip surfaces (sample Mi0707, Figure 8c).

5. Discussion

From the data presented in this study, we reconstructed a complex shear-related deformation history in spite of the low strain accumulated by the studied fault. Petrographic observations and mass balance calculations demonstrate that pressure solution was an effective deformation mechanism during the Millaris thrust activity, with a massive departure of calcite from the fault rocks and a more limited mobility of quartz (Figure 6). Such a mobility difference could be explained by the temperature and pressure conditions, and the fluid chemistry. At the pressure-temperature (*P-T*) conditions estimated for the deformation of the Millaris fault (~260°C, ~7 km depth), calcite and quartz are both soluble components of the rock, with calcite being slightly more soluble than quartz for $T <$ ~300°C [e.g., *Gratier et al.,* 2013]. The concentration of other dissolved species such as CO_2 and NaCl could also influence both mineral solubilities [*Brantley,* 1992; *Fein and Walther,* 1987; *Newton and Manning,* 2000, 2002]. At constant *P* and *T* calcite is more soluble in fluid with increasing NaCl concentration whereas quartz shows the opposite behavior [*Brantley,* 1992]. In a previous study focusing on fluid inclusions from the Millaris thrust fault, *Lacroix et al.* [2011] suggested the presence of a NaCl-bearing brines in fluid inclusions. Therefore, the difference of mobility observed between calcite and quartz is more likely associated to the fluid chemistry, and the presence of NaCl, rather than *P-T* conditions.

Our mass balance calculations indicate that a volume loss up to ~50%, supposedly associated to calcite pressure solution, occurred in the Millaris fault rocks despite its low displacement (<30 m). This volume loss, with higher departure along shear surfaces than inside sigmoidal tectonites, suggests that fault-related deformation, and possibly deformation-enhanced fluid flow, has a profound effect on pressure solution, in agreement with previous studies [*Gratier and Gamond*, 1990; *Bos et al.,* 2000; *Bos and Spiers*, 2001] and confirms the catalytic role of phyllosilicates in speeding up pressure solution-related deformation [e.g., *Renard et al.,* 1997; *Aharonov and Katsman*, 2009; *Viti et al.,* 2014].

The calcite removed from the fault system is likely to be redeposited, at least partially, at the host rock-fault zone interface where thick shear veins are observed (Figure 3c). Such volume loss from the fault rocks induced the concentration and realignment of insoluble phyllosilicates along preferential fabrics (C, C′, and S), and the creation of an anastomosed network of shear bands. Newly formed chlorite has been identified along shear surfaces from the fault core, suggesting that recrystallization process occurred during deformation. Although no clear evidence of synkinematic illite has been observed in the Millaris thrust, *Buatier et al.* [2012] demonstrated that illite recrystallization occurred during deformation along the Monte Perdido thrust, located several hundred meters below the studied area. Therefore, illite recrystallization could be envisaged. More in general, the low variations of elements composing the phyllosilicates (e.g., Si, Al, Fe, and Mg) (Figures 6 and 7b) indicate that illite and chlorite could have experienced, together with quartz, only local recrystallization phenomena along the shear surfaces without substantial mass transfers beyond the boundaries of the shear zone and, as a consequence, be regarded as largely immobile.

In addition, the lack of angular clasts and the absence of grain size reduction during deformation suggest that there was only minor competition of cataclasis with pressure solution as in the case of other fault zones localized in phyllosilicate-rich rock [e.g., *Alvarez et al.,* 1978; *Gratier et al.,* 2011; *Tesei et al.,* 2013].

On the basis of field evidence, the Millaris fault accommodated a maximum displacement of about 30 m. Assuming a simple shear strain geometry, this yields a $\Upsilon \sim 3$. However, this computation makes the assumption that the shear zone did not experience volume loss [*Ramsay*, 1967, 1980]. Volume loss could complicate the shear strain calculation and overestimate it [*Ramsay and Wood*, 1973; *Tikoff and Fossen,* 1993; *Fagereng,* 2013; *Baird and Hudleston,* 2007]. Considering volume loss between 20% and 45%, as suggested by our mass balance estimation, and pressure solution surface oriented at 45° to the shear surfaces, the initial fault width was likely between 11 and 17 m. Therefore, the corrected shear strain associated with simple shear only should vary between 1.7 and 2.8 depending to the considered volume loss.

Slickenlines and slickenfibers observed on natural shear surfaces demonstrate that sliding along phyllosilicate horizons was another active deformation mechanism in the fault zone and they are related to simple shear sliding. Likewise, the same process of frictional sliding has been observed during our experiments, and it is responsible for the apparent weakness of the Millaris foliated fault rocks. Therefore, we propose that most of the simple shear experienced by the Millaris fault rocks might be explained by a combination of pressure solution creep and frictional sliding along the foliation.

Our mechanical measurements demonstrate that the Millaris detachment nucleated in an inherently weak formation (Millaris marls, $\mu \approx 0.4$) and, as soon as the fault zone developed, pressure solution creep helps to concentrate phyllosilicates along the fault zone resulting in a drop of the frictional strength ($\mu < 0.3$). Higher frictional healing rates measured in the host sediments reinforce the interpretation that the sliding within the parent marls could have been locked after the development of the fault rocks that are significantly weaker and show null postslip restrengthening (e.g., Figure 8b).

We propose that brittle faulting took place in the Millaris marls due to their inherent weakness with respect to the surrounding rocks (e.g., Figure 8a). Then, the increase of fault permeability during the deformation as well as the presence of phyllosilicates acted as catalysts favoring pressure solution and massive volume loss. Once developed, the fault zone fabric with continuous phyllosilicate horizons, sliding along the foliation was probably the preferred deformation mechanism substituting the pressure solution creep. Alternatively, it is possible to hypothesize that pressure solution creep, which causes the thickening of phyllosilicate-rich horizons, and the frictional sliding along the foliation, resulting in the thinning of the same horizons, where cyclically active in the fault zone, consistently with previous observations in other fault zones [e.g.,

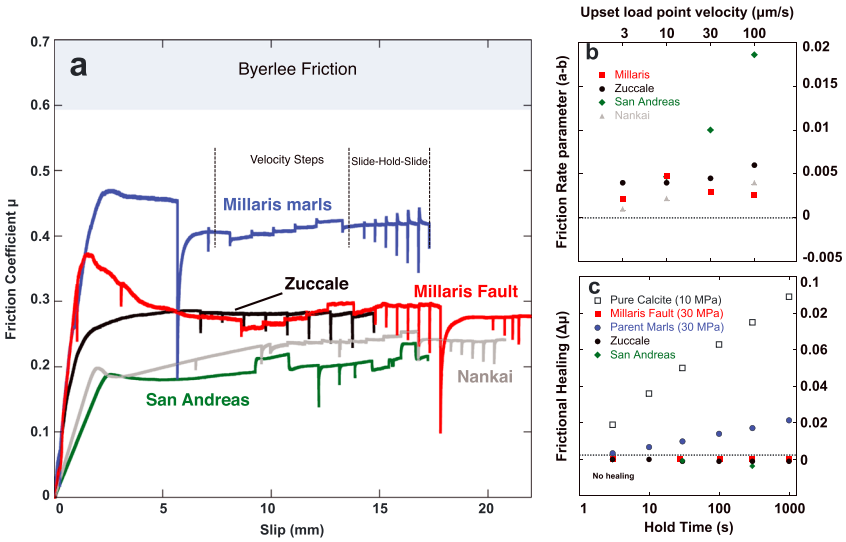

Figure 9. Friction comparison between Millaris incipient thrust and other major faults. (a) Friction versus shear displacement curves for representative samples of the Millaris marls (blue), the Millaris incipient thrust (red), the Zuccale low-angle normal fault [*Tesei et al.,* 2012] (black), the Nankai megasplay thrust [*Ikari and Saffer,* 2011] (grey), and the San Andreas strike-slip fault from SAFOD borehole [*Lockner et al.,* 2011] (green). Effective normal stress is similar for all samples (σ'_n = 10–30 MPa for Millaris thrust, σ'_n = 25 MPa San Andreas and Nankai, σ'_n = 20 MPa Zuccale). All experiments from fault core rocks show a similar low friction $\mu < 0.3$. Byerlee friction is shown for comparison. (b) Frictional stability parameters (*a-b*) of fault core rocks display positive values suggesting stable sliding behavior. (c) Healing rates comparison: fault rocks from the Millaris thrust and major faults lack of frictional restrengthening. Healing of Millaris marls and pure calcite are shown for comparison.

Alvarez et al., 1978; *Tesei et al.,* 2013; *Meere et al.,* 2013; *Gratier et al.,* 2011]. In both cases, the sliding along the Millaris thrust was probably aseismic, since both pressure solution creep and frictional sliding along the phyllosilicates should have favored stable deformation.

Frictional strength of intact fault samples from the Millaris thrust tested reproducing their in situ shear geometry, $\mu = 0.27$, is comparable to the friction values measured for the rocks of major weak faults such as the San Andreas [*Lockner et al.,* 2011; *Carpenter et al.,* 2011], the Zuccale normal fault [*Tesei et al.,* 2012], and the Nankai décollement [*Ikari and Saffer,* 2011] ($\mu < 0.3$, Figure 9a). In addition, the comparison of rate state constitutive parameters (Figure 9b) and healing properties (Figure 9c) indicate also a similar slip behavior characterized by stable, velocity strengthening sliding without significant restrengthening during quasi-static loading periods.

This study demonstrates that the onset of fault weakening, favored by dissolution of strong mineral phases and concentration of weak phyllosilicate-rich material, can occur at the very beginning of the fault's activity. However, not all the faults are prone to develop early weakening processes. Our studies indicate that incipient fault weakening is favored in sedimentary detachment levels such as marls or shales that are rich of both high-solubility minerals and phyllosilicates.

6. Conclusions

We document the chemical and the mechanical evolution of an incipient thrust fault coupling mineralogy and geochemistry to friction experiments. Our results demonstrate that in carbonatic sequences, fluid-assisted stress-driven volume loss resulting in high concentration of weak mineral phases (illite and chlorite), allowed a significant reduction in the fault strength from the early stages of the activity. This implies that fault weakness is not a mechanical property of mature faults only, but it can be also a characteristic of small displacement structures, especially in faults originating from lithologies rich in phyllosilicates and soluble minerals, such as shales or marls. This weakness likely controls the birth of tectonic décollements in compressional regimes allowing the efficient decoupling of the various tectonic units along weak, and potentially aseismic, faults.

Acknowledgments
This research was realized within the framework of the ERC starting grant GLASS project (grant 259256) and the FNS project 20020-126973/1. We thank B.M. Carpenter and M.J. Ikari for providing raw experimental data for the comparisons. We also acknowledge the careful editorial handling of D. Grujic and J. Geissman and thorough reviews from J.-P. Gratier and A. Fagereng. The data for this paper are available by contacting the corresponding author.

References

Aharonov, E., and R. Katsman (2009), Interaction between pressure solution and clays in stylolite development: Insights from modeling, *Am. J. Sci.*, *309*, 607–632, doi:10.2475/07.2009.04.

Alvarez, W., T. Engelder, and P. A. Geiser (1978), Classification of solution cleavage in pelagic limestones, *Geology*, *6*, 263–266.

Baird, G. B., and P. J. Hudleston (2007), Modeling the influence of tectonic extrusion and volume loss on the geometry, displacement, vorticity, and strain compatibility of ductile shear zones, *J. Struct. Geol.*, *29*, 1665–1678, doi:10.1016/j.jsg.2007.06.012.

Baumgartner, L. P., and S. N. Olsen (1995), A least-squares approach to mass transport calculations using the isocon method, *Econ. Geol.*, *90*, 1261–1270.

Berthé, D., P. Choukroune, and P. Jegouzo (1979), Orthogneiss, mylonite and non coaxial deformation of granites: The example of the South Armorican Shear Zone, *J. Struct. Geol.*, *1*, 31–42, doi:10.1016/0191-8141(79)90019-1.

Bos, B., and C. J. Spiers (2001), Experimental investigation into the microstructural and mechanical evolution of phyllosilicate-bearing fault rock under conditions favouring pressure solution, *J. Struct. Geol.*, *23*, 1187–1202, doi:10.1016/S0191-8141(00)00184-X.

Bos, B., C. J. Peach, and C. J. Spiers (2000), Frictional-viscous flow of simulated fault gouge caused by the combined effects of phyllosilicates and pressure solution, *Tectonophysics*, *327*, 173–194, doi:10.1016/S0040-1951(00)00168-2.

Brantley, S. L. (1992), The effect of fluid chemistry on quartz microcrack lifetimes, *Earth Planet. Sci. Lett.*, *113*, 145–156, doi:10.1016/0012-821X(92)90216-I.

Buatier, M., B. Lacroix, P. Labaume, V. Moutarlier, D. Charpentier, J. P. Sizun, and A. Travé (2012), Microtextural investigation (SEM and TEM study) of phyllosilicates in a major thrust fault zone (Monte Perdido, southern Pyrenees): Impact on fault reactivation, *Swiss J. Geosci.*, *105*, 313–324, doi:10.1007/s00015-012-0098-0.

Byerlee, J. (1978), Friction of rocks, *Pure Appl. Geophys.*, *116*, 615–626.

Carpenter, B. M., C. Marone, and D. M. Saffer (2011), Weakness of the San Andreas Fault revealed by samples from the active fault zone, *Nat. Geosci.*, *4*, 251–254.

Chester, F. M., J. P. Evans, and R. L. Biegel (1993), Internal structure and weakening mechanisms of the San Andreas Fault, *J. Geophys. Res.*, *98*, 771–786, doi:10.1029/92JB01866.

Collettini, C., and R. H. Sibson (2001), Normal faults, normal friction?, *Geology*, *29*, 927–930.

Collettini, C., A. Niemeijer, C. Viti, and C. Marone (2009), Fault zone fabric and fault weakness, *Nature*, *462*, 907–910.

Collettini, C., A. R. Niemeijer, C. Viti, S. A. F. Smith, and C. Marone (2011), Fault structure, frictional properties and mixed-mode fault slip behaviour, *Earth Planet. Sci. Lett.*, *311*, 316–327, doi:10.1016/j.epsl.2011.09.020.

Collettini, C., G. Di Stefano, B. Carpenter, P. Scarlato, T. Tesei, S. Mollo, F. Trippetta, C. Marone, G. Romeo, and L. Chiaraluce (2014), A novel and versatile apparatus for brittle rock deformation, *Int. J. Rock Mech. Min. Sci.*, *66*, 114–123.

Cubas, N., J. P. Avouac, P. Souloumiac, and Y. Leroy (2013), Megathrust friction determined from mechanical analysis of the forearc in the Maule earthquake area, *Earth Planet. Sci. Lett.*, *381*, 92–103.

Dieterich, J. H. (1972), Time-dependent friction in rocks, *J. Geophys. Res.*, *77*, 3690–3697, doi:10.1029/JB077i020p03690.

Fagereng, Å. (2013), On stress and strain in a continuous-discontinuous shear zone undergoing simple shear and volume loss, *J. Struct. Geol.*, *50*, 44–53, doi:10.1016/j.jsg.2012.02.016.

Fagereng, A., F. Remitti, and R. H. Sibson (2010), Shear veins observed within anisotropic fabric at high angles to the maximum compressive stress, *Nat. Geosci.*, *3*, 482–485.

Fein, J. B., and J. V. Walther (1987), Calcite solubility in supercritical CO_2-H_2O fluids, *Geochim. Cosmochim. Acta*, *51*, 1665–1673, doi:10.1016/0016-7037(87)90346-2.

Gratier, J. P., and J. F. Gamond (1990), Transition between seismic and aseismic deformation in the upper crust, *Geol. Soc. London, Spec. Publ.*, *54*, 461–473, doi:10.1144/GSL.SP.1990.054.01.42.

Gratier, J.-P., J. Richard, F. Renard, S. Mittempergher, M. L. Doan, G. Di Toro, J. Hadizadeh, and A. M. Boullier (2011), Aseismic sliding of active faults by pressure solution creep: Evidence from the San Andreas Fault observatory at depth, *Geology*, *39*, 1131–1134.

Gratier, J.-P., D. K. Dysthe, and F. Renard (2013), Chapter 2: The role of pressure solution creep in the ductility of the Earth's upper crust, in *Advances in Geophysics*, edited by R. Dmowska, pp. 47–179, Elsevier.

Holdsworth, R. E. (2004), Weak faults-rotten cores, *Science*, *303*, 81–182.

Hubbert, K., and M. Rubey (1959), Role of fluid pressure in mechanics of overthrust faulting, *Geol. Soc. Am. Bull.*, *70*, 115–166, doi:10.1130/0016-7606(1959)70[115:ROFPIM]2.0.CO;2.

Ikari, M. J., and D. M. Saffer (2011), Comparison of frictional strength and velocity dependence between fault zones in the Nankai accretionary complex, *Geochem. Geophys. Geosyst.*, *12*, Q0AD11, doi:10.1029/2010GC003442.

Lacroix, B., M. Buatier, P. Labaume, A. Travé, M. Dubois, D. Charpentier, S. Ventalon, and D. Convert-Gaubier (2011), Microtectonic and geochemical characterization of thrusting in a foreland basin: Example of the South-Pyrenean orogenic wedge (Spain), *J. Struct. Geol.*, *33*, 1359–1377.

Lacroix, B., D. Charpentier, M. Buatier, T. Vennemann, P. Labaume, T. Adatte, A. Travé, and M. Dubois (2012), Formation of chlorite during thrust fault reactivation. Record of fluid origin and P–T conditions in the Monte Perdido thrust fault (southern Pyrenees), *Contrib. Mineral. Petrol.*, *163*, 1083–1102.

Lahfid, A., O. Beyssac, E. Deville, F. Negro, C. Chopin, and B. Goffé (2010), Evolution of the Raman spectrum of carbonaceous material in low-grade metasediments of the Glarus Alps (Switzerland), *Terra Nova*, *22*, 354–360, doi:10.1111/j.1365-3121.2010.00956.x.

Lockner, D. A., C. Morrow, D. Moore, and S. Hickman (2011), Low strength of deep San Andreas Fault gouge from SAFOD core, *Nature*, *472*, 82–85.

Marone, C. (1998), Laboratory-derived friction laws and their application to seismic faulting, *Annu. Rev. Earth Planet. Sci.*, *26*, 643–696.

Massironi, M., A. Bistacchi, and L. Menegon (2011), Misoriented faults in exhumed metamorphic complexes: Rule or exception?, *Earth Planet. Sci. Lett.*, *307*, 233–239, doi:10.1016/j.epsl.2011.04.041.

Meere, P. A., K. F. Mulchrone, and M. Timmerman (2013), Shear folding in low-grade metasedimentary rocks: Reverse shear along cleavage at a high angle to the maximum compressive stress, *Geology*, *41*, 879–882, doi:10.1130/G34150.1.

Moore, D. E., and M. J. Rymer (2007), Talc-bearing serpentinite and the creeping section of the San Andreas Fault, *Nature*, *448*, 795–797, doi:10.1038/nature06064.

Newton, R. C., and C. E. Manning (2000), Quartz solubility in H_2O-NaCl and H_2O-CO_2 solutions at deep crust-upper mantle pressures and temperatures: 2–15 kbar and 500–900°C, *Geochim. Cosmochim. Acta*, *64*, 2993–3005, doi:10.1016/S0016-7037(00)00402-6.

Newton, R. C., and C. E. Manning (2002), Experimental determination of calcite solubility in H_2O-NaCl solutions at deep crust/upper mantle pressures and temperatures: Implications for metasomatic processes in shear zones, *Am. Mineral.*, *87*, 1401–1409.

Ramsay, J. G. (1967), *Folding and Fracturing of Rocks, International Series in the Earth and Planetary Sciences*, 568 pp., McGraw-Hill, New York.

Ramsay, J. G. (1980), Shear zone geometry: A review, *J. Struct. Geol.*, *2*, 83–99, doi:10.1016/0191-8141(80)90038-3.
Ramsay, J. G., and D. S. Wood (1973), The geometric effects of volume change during deformation processes, *Tectonophysics*, *16*, 263–277, doi:10.1016/0040-1951(73)90015-2.
Remacha, E., and L. P. Fernandez (2003), High-resolution correlation patterns in the turbidite systems of the Hecho Group (South-Central Pyrenees, Spain), *Mar. Pet. Geol.*, *20*, 711–726, doi:10.1016/j.marpetgeo.2003.09.003.
Renard, F., P. Ortoleva, and J. P. Gratier (1997), Pressure solution in sandstones: Influence of clays and dependence on temperature and stress, *Tectonophysics*, *280*, 257–266, doi:10.1016/S0040-1951(97)00039-5.
Scuderi, M. M., A. R. Niemeijer, C. Collettini, and C. Marone (2013), Frictional properties and slip stability of active faults within carbonate–evaporite sequences: The role of dolomite and anhydrite, *Earth Planet. Sci. Lett.*, *369–370*, 220–232.
Sibson, R. H., and G. Xie (1998), Dip range for intracontinental reverse fault ruptures: Truth not stranger than friction?, *Bull. Seismol. Soc. Am.*, *88*, 1014–1022.
Suppe, J. (2007), Absolute fault and crustal strength from wedge tapers, *Geology*, *35*, 1127–1130.
Teixell, A. (1996), The Anso transect of the southern Pyrenees: Basement and cover thrust geometries, *J. Geol. Soc.*, *153*, 301–310, doi:10.1144/gsjgs.153.2.0301.
Tesei, T., C. Collettini, B. M. Carpenter, C. Viti, and C. Marone (2012), Frictional strength and healing behavior of phyllosilicate-rich faults, *J. Geophys. Res.*, *117*, B09402, doi:10.1029/2012JB009204.
Tesei, T., C. Collettini, C. Viti, and M. R. Barchi (2013), Fault architecture and deformation mechanisms in exhumed analogues of seismogenic carbonate-bearing thrusts, *J. Struct. Geol.*, *55*.
Tesei, T., C. Collettini, M. R. Barchi, B. M. Carpenter, and G. Di Stefano (2014), Heterogeneous strength and fault zone complexity of carbonate-bearing thrusts with possible implications for seismicity, *Earth Planet. Sci. Lett.*, *408*, 307–318.
Tikoff, B., and H. Fossen (1993), Simultaneous pure and simple shear: The unifying deformation matrix, *Tectonophysics*, *217*, 267–283, doi:10.1016/0040-1951(93)90010-H.
Torgersen, E., and G. Viola (2014), Structural and temporal evolution of a reactivated brittle-ductile fault—Part I: Fault architecture, strain localization mechanisms and deformation history, *Earth Planet. Sci. Lett.*, *407*, 205–220.
Townend, J., and M. D. Zoback (2000), How faulting keeps the crust strong, *Geology*, *28*, 399–402.
Vidal, O., T. Parra, and F. Trotet (2001), A thermodynamic model for Fe-Mg aluminous chlorite using data from phase equilibrium experiments and natural pelitic assemblages in the 100° to 600°c, 1 to 25 kb range, *Am. J. Sci.*, *301*, 557–592, doi:10.2475/ajs.301.6.557.
Vidal, O., T. Parra, and P. Vieillard (2005), Thermodynamic properties of the Tschermak solid solution in Fe-chlorite: Application to natural examples and possible role of oxidation, *Am. Mineral.*, *90*, 347–358.
Vidal, O., V. De Andrade, E. Lewin, M. Munoz, T. Parra, and S. Pascarelli (2006), P–T-deformation-Fe^{3+}/Fe^{2+} mapping at the thin section scale and comparison with XANES mapping: Application to a garnet-bearing metapelite from the Sambagawa metamorphic belt (Japan), *J. Metamorph. Geol.*, *24*, 669–683, doi:10.1111/j.1525-1314.2006.00661.x.
Viti, C., C. Collettini, and T. Tesei (2014), Pressure solution seams in carbonatic fault rocks: Mineralogy, micro/nanostructures and deformation mechanism, *Contrib. Mineral. Petrol.*, *167*, 1–15, doi:10.1007/s00410-014-0970-1.
Willemse, E. J. M., D. C. P. Peacock, and A. Aydin (1997), Nucleation and growth of strike- slip faults in limestone from Somerset, UK, *J. Struct. Geol.*, *19*, 1461–1477, doi:10.1016/S0191-8141(97)00056-4.
Wintsch, R. P., R. Christoffersen, and A. K. Kronenberg (1995), Fluid-rock reaction weakening of fault zones, *J. Geophys. Res.*, *100*, 13,021–13,032, doi:10.1029/94JB02622.
Zoback, M. D., et al. (1987), New evidence on the state of stress of the San Andreas Fault system, *Science*, *238*, 1105–1111.